

Correlated vs. conventional insulating behavior in the $J_{\text{eff}} = 1/2$ vs. $3/2$ bands in the layered iridate Ba_2IrO_4

M. Uchida,^{1,*} Y.F. Nie,^{1,2} P.D.C. King,^{1,3} C.H. Kim,⁴
C.J. Fennie,⁴ D.G. Schlom,^{2,3} and K.M. Shen^{1,3,†}

¹*Laboratory of Atomic and Solid State Physics, Department of Physics,
Cornell University, Ithaca, New York 14853, USA*

²*Department of Materials Science and Engineering,
Cornell University, Ithaca, New York 14853, USA*

³*Kavli Institute at Cornell for Nanoscale Science, Ithaca, New York 14853, USA*

⁴*Department of Applied Physics, Cornell University, Ithaca, New York 14853, USA*

(Dated: April 29, 2019)

Abstract

We employ molecular beam epitaxy to stabilize Ba_2IrO_4 thin films and utilize *in situ* angle-resolved photoemission spectroscopy to investigate the evolution of its electronic structure through the Néel temperature T_N . Our measurements indicate that dispersions of the relativistic $J_{\text{eff}} = 1/2$ and $3/2$ bands exhibit an unusual dichotomy in their behavior through the Néel transition. Although the charge gap survives into the paramagnetic state, only the $J_{\text{eff}} = 1/2$ state exhibits a strong temperature dependence and its gap softens with increasing temperature approaching T_N , while the nearly fully occupied $J_{\text{eff}} = 3/2$ state which remains nearby in energy exhibits negligible changes with temperature.

PACS numbers: 71.30.+h, 74.25.Jb, 71.70.Ej, 71.20.-b

I. INTRODUCTION

$5d$ transition metal oxides have recently attracted great interest due to the interplay between spin-orbit and Coulomb interactions which can give rise to novel many-body quantum states, including the theoretically proposed Weyl semimetal,^{1,2} topological Mott insulator,^{3,4} or high-temperature superconductivity upon carrier doping.^{5,6} These studies have been largely motivated by the experiments in a model compound Sr_2IrO_4 , which suggest that the low-energy electronic states can be suitably represented by their effective total angular momentum J_{eff} , and argue that the Ir^{4+} ($5d^5$) t_{2g} orbitals are split into a fully filled $J_{\text{eff}} = 3/2$ manifold and a singly occupied $J_{\text{eff}} = 1/2$ band.^{7,8} It has been proposed that the modest Coulomb interactions of the $5d$ electrons can then result in a further splitting of the half-filled $J_{\text{eff}} = 1/2$ band into a fully occupied valence band and an unoccupied conduction band.

At present, there remains considerable debate about whether iridates are better described as Mott insulators,⁹ in analogy to the conventional $3d$ transition metal oxides, or as Slater insulators,¹⁰⁻¹² where the insulating behavior is tied directly to long-range antiferromagnetic order. For example, recent scanning tunnel spectroscopy on Sr_2IrO_4 has reported an onset of the temperature dependent spectra below the antiferromagnetic ordering temperature T_N , consistent with dynamical mean field theory results,¹² although the in-gap spectral weight is still strongly suppressed even above T_N , as also seen in other spectroscopy experiments.^{9,10} In order to definitively address these issues, it has become critical to systematically examine other related $5d$ transition metal oxides, such as Ba_2IrO_4 . This also opens new avenues to realize proposed exotic phases such as superconductivity which may exist at the intersection between strong spin-orbit interactions and electron correlations.

Ba_2IrO_4 is an ideal candidate material for addressing many of the outstanding issues in the field of the iridates. Ba_2IrO_4 possesses a less distorted, simple quasi-two-dimensional crystal structure ($I4/mmm$ in bulk), as shown in Fig. 1(a), with Ba replacing Sr,¹³ while it shows the same insulating behavior accompanied with the basal plane antiferromagnetic order below the Néel temperature $T_N = 240$ K.¹⁴ The undistorted crystal structure without the in-plane IrO_6 octahedral rotation is expected to result in simplified band dispersions without folded features, enabling us to follow the detailed temperature evolution of the relativistic $J_{\text{eff}} = 1/2$ and $3/2$ bands and to determine their roles in the formation of the insulating

phase. In addition, Ba_2IrO_4 has a number of distinct advantages over Sr_2IrO_4 , including the capacity for being metallized either through carrier doping (K or La substitution for Ba)¹⁵ or through the application of hydrostatic pressure,¹⁶ making it an excellent platform for searching for the possibility of exotic, iridate-based superconductivity. Unfortunately, layered Ba_2IrO_4 is metastable in bulk and can only be formed under high pressure, making the synthesis of large bulk single crystals difficult. Here, we apply oxide molecular beam epitaxy (MBE) to stabilize thin films of the desired structure of Ba_2IrO_4 , and utilize *in situ* angle-resolved photoemission spectroscopy (ARPES) to investigate the parent insulating ground state of Ba_2IrO_4 and how it evolves through T_N . Longitudinal in-plane resistivity in Fig. 1(b) shows clear insulating characteristics of the Ba_2IrO_4 film. We compare our ARPES measurements with calculations based on density functional theory incorporating electron-electron and spin-orbit interactions. While both the relativistic $J_{\text{eff}} = 1/2$ and $3/2$ states are nearly degenerate near E_F , we reveal a surprising contrast in their temperature dependence. Although the gap survives well into the paramagnetic state, only the $J_{\text{eff}} = 1/2$ band exhibits a substantial broadening and ‘softening’ of the gap with increasing temperature approaching T_N reminiscent of some of the parent cuprate superconductors,²² suggesting the importance of long-range antiferromagnetic order.

II. EXPERIMENTAL AND CALCULATIONAL PROCEDURES

Thin films of (001) Ba_2IrO_4 of thickness ~ 15 nm were deposited epitaxially on (001)_{*p*} (where the subscript *p* denotes pseudocubic indices) PrScO_3 single crystal substrates using a Veeco GEN10 oxide MBE system. Absorption-controlled deposition was performed in distilled 100% O_3 at a background pressure of 1×10^{-6} Torr. Under optimized adsorption controlled conditions, Ba and Ir were supplied continuously with a flux of 6×10^{12} and 7×10^{12} atoms/cm²s from an effusion cell and an electron beam evaporator, respectively. The substrate was heated at 800 °C as measured by a pyrometer. Under these conditions the extra Ir atoms form volatile IrO_x ¹⁷ and then evaporate from the surface, leaving stoichiometric Ba_2IrO_4 films.

During growth films were monitored with reflection high-energy electron diffraction (RHEED) while rotating the substrate. After growth, samples were immediately (< 300 seconds) transferred through ultrahigh vacuum to a high-resolution ARPES system. Mea-

measurements were performed using a VUV5000 helium plasma discharge lamp and a VG Scienta R4000 hemispherical electron spectrometer, with an excitation energy of 21.2 eV (He I α) and an instrumental energy resolution of 20 meV. The sample was measured at temperatures between 100 and 300 K while maintaining a base pressure typically better than 8×10^{-11} Torr. Following ARPES measurements, films were characterized *in situ* by low-energy electron diffraction (LEED). The phase purity and crystallinity of Ba₂IrO₄ films were characterized also using *ex situ* four-circle x-ray diffraction (XRD) with Cu $K\alpha$ radiation.

The *ab-initio* density functional theory (DFT) calculations were performed using Wien2k code¹⁸ including spin-orbit coupling and an on-site Coulomb repulsion, with the local density approximation and the Perdew-Burke-Ernzerhof exchange-correlation functional.¹⁹ A tetragonal structure was assumed, with the slightly strained lattice ($a = 4.021$ Å and $c = 13.34$ Å) on the PrScO₃ substrate, and no peaks corresponding to octahedral rotation were observed from bulk diffraction measurements.

III. FILM CHARACTERIZATION

Figure 2 shows typical RHEED images of the PrScO₃ substrate and Ba₂IrO₄ film along the [110]_(p) and [100]_(p) azimuth. Ba₂IrO₄ films exhibit prominent Kikuchi lines, indicating high crystalline perfection, ensuring the quality of the photoemission spectra. The in-plane lattice mismatch to the PrScO₃ substrate ($a_p = 4.021$ Å) induces only 0.2% compressive strain and the RHEED streaks do not show a discernible shift resulting from any lattice relaxation (Figs. 2(c) and (f)).

Exemplary LEED patterns are shown in Figs. 3(a) and (b), taken at normal incidence with beam energies of 150 and 200 eV. The sharp diffraction peaks indicate a well ordered surface crystal structure. The assumed tetragonal (1×1) diffraction peaks are indicated in the pattern, and weak Bragg peaks observed at $\sqrt{2} \times \sqrt{2}$ R45° relative to the 1×1 peaks are likely a result of an in-plane surface reconstruction in Ba₂IrO₄, given the absence of such peaks in bulk x-ray measurements. The XRD θ - 2θ scan in Fig. 3(c) shows clear Kiessig fringes, indicating good surface smoothness, and a Nelson-Riley analysis of the peak positions gives an out-of-plane lattice constant of $c = 13.34$ Å, meaning films may be slightly elongated along the c -axis compared with bulk polycrystals ($a = 4.030$ Å and $c = 13.333$ Å)¹³ due to the compressive in-plane strain.

IV. RESULTS AND DISCUSSION

Figures 4(a)-(c) show valence band photoemission spectra at high-symmetry points for Ba₂IrO₄ epitaxial films. By comparison to calculations,^{7,11,20,21} the peaks near the Fermi level E_F can be assigned to the Ir 5d t_{2g} bands, while the spectral features between 2 and 7 eV can be ascribed to dominantly O 2p states. As shown in the energy distribution curves (EDCs) in Fig. 4(d), low-energy dispersive features with clearly defined peaks are observed close to E_F , where the lowest-energy feature is located ~ 0.3 eV below centered at the $(\pi, 0)$ point, with another peak at the (π, π) point only 0.4 eV below E_F . The full width at half maximum of the EDC peaks were typically ~ 200 meV near the top of the valence band, with a lineshape well fit by a Gaussian. This indicates that the broad spectra are dominated by a manifold of states that involve multiple bosonic excitations, suggesting polaronic behavior, similar to that observed in the insulating parent cuprates,²² as well as in the sister compound Sr₂IrO₄.²³

In Figure 5, we compare the near- E_F ARPES spectra and the experimental dispersions (Σ_1 - Σ_3) extracted from EDC and momentum distribution curve (MDC) fits, to our DFT calculations with spin-orbit coupling and an on-site Coulomb repulsion U . As shown in Fig. 5(a), along the $(\pi, 0)$ - (π, π) or $(\pi/2, \pi/2)$ - (π, π) high symmetry directions, the half-filled Σ_1 band exhibits clear back-bending, indicating that a full gap opens along the $(\pi, 0)$ - $(0, \pi)$ diagonal line, consistent with (π, π) Néel antiferromagnetic order which is experimentally observed.⁸ The lowest energy states are at $(\pi, 0)$, where the peak position is at a binding energy of approximately 0.3 eV, consistent with earlier ARPES measurements on bulk Sr₂IrO₄ and Ba₂IrO₄ single crystals.^{7,24} Comparisons to our DFT calculations with U of 2.5 eV (comparable to values reported in the literature for Sr₂IrO₄^{7,20,29}) give qualitatively good agreement with the experimental dispersions, and indicate that the Σ_1 states which open a gap near $(\pi, 0)$ are of predominately $J_{\text{eff}} = 1/2$ character. The Σ_2 and Σ_3 states near (π, π) are observed to be very close in energy to the $(\pi, 0)$ states, and in fact form the lowest lying states in the predicted valence band maximum at (π, π) , at odds with experiment, but also observed in previous works on Sr₂IrO₄.^{7,29} Comparisons with the DFT calculations indicate that these states are of predominately $J_{\text{eff}} = 3/2$ character; the J_{eff} character of these states do not appear to depend strongly on U (Figs. 5(b) and (c)) or octahedral rotation angle, consistent with earlier work on Sr₂IrO₄ by Martins *et al.*²⁰ This

underscores the importance of low-lying $J_{\text{eff}} = 3/2$ states in the low energy physics of the layered iridates, and that the bandwidth of the $J_{\text{eff}} = 1/2$ and $3/2$ states is substantially larger than their splittings. The faint dispersion especially around 0.5 eV centered at $(0, 0)$ is likely a folded feature of the corresponding Σ_2 band at (π, π) , which is probably due to the $\sqrt{2} \times \sqrt{2}$ in-plane surface structural distortion observed in the LEED images (Figs. 3(a) and (b)). However, the effect of this reconstruction on the observed electronic structure appears much smaller than in Sr_2IrO_4 , in that the intensity of the reflected shadow band around $(0, 0)$ is significantly weaker than at (π, π) , whereas in Sr_2IrO_4 the intensity of these features are comparable. This may also imply that the octahedral rotation angles observed at the surface of the Ba_2IrO_4 films are substantially smaller than those in Sr_2IrO_4 .^{25,26}

Here it is meaningful to quantitatively compare the observed energy bands with the calculated ones. The experimentally extracted bandwidths (separation from band minimum to maximum) are $W_{\Sigma_1(0,0)-(\pi,0)} = 0.9 \pm 0.1$ eV, $W_{\Sigma_2(0,0)-(\pi,0)} = 0.7 \pm 0.1$ eV, $W_{\Sigma_2(\pi,0)-(\pi,\pi)} = 0.5 \pm 0.1$ eV, and $W_{\Sigma_3(\pi,0)-(\pi,\pi)} = 1.1 \pm 0.1$ eV. On the other hand, the corresponding values in the DFT calculations with U of 2.5 eV are 0.74 eV, 0.68 eV, 0.48 eV, and 1.16 eV, respectively. Setting U to zero only increases these bandwidths slightly to 1.13 eV, 0.93 eV, 0.54 eV, and 1.48 eV, but this weak renormalization reflects the relatively modest effective Coulomb interaction of the $5d$ electrons, in contrast to the much larger bandwidth renormalization typically observed in the high- T_c cuprates. The other remarkable point is the energy difference between the Σ_1 and Σ_2 bands. Since this gap at the Γ point directly measures the spin-orbit coupling parameter as suggested by tight-binding models,^{21,27} the spin-orbit interaction in Ba_2IrO_4 is experimentally determined to be 0.5 ± 0.1 eV, which is also consistent to the reports on other iridate systems.^{7,28}

Figure 6 shows a comparison of the measured low-energy electronic structures of Ba_2IrO_4 and Sr_2IrO_4 . (001) Sr_2IrO_4 films were epitaxially grown on LSAT substrates by MBE, with the ARPES spectra consistent with previous measurements.^{7,29} As shown in Fig. 6(d), the Brillouin zone of Sr_2IrO_4 is reduced by half in momentum space and the band structure is folded along the $(\pi, 0)$ - $(0, \pi)$ and equivalent diagonal lines, reflecting the $\sqrt{2} \times \sqrt{2}$ in-plane distortion illustrated in Fig. 6(e). The folded bands are more clearly visible in the E versus k plots shown in Figs. 6(c) and (f). For example, the band dispersion seen centered at (π, π) in Ba_2IrO_4 can be clearly observed at the equivalent reconstructed position $(0, 0)$ in the case of Sr_2IrO_4 . We interpret the weaker reconstruction observed in Ba_2IrO_4 as an indication

that the amount of octahedral rotation due to the surface reconstruction is significantly less than in Sr_2IrO_4 . In addition, we find that the total bandwidth of the t_{2g} bands are about 1.4 eV both in Ba_2IrO_4 and Sr_2IrO_4 . This suggests that the transfer integrals between the nearest-neighbor d_{xy} (d_{yz} , d_{zx}) orbitals are roughly comparable.

Given that the $J_{\text{eff}} = 1/2$ and $3/2$ states are nearly degenerate near E_F , we investigated their roles in the Néel transition by tracking their temperature dependence through T_N . Figure 7(a) shows temperature-dependent EDCs at the different momentum positions A–C sketched in Fig. 7(c). The spectra change reproducibly both in warming and cooling, ruling out the possibility of sample surface degradation. The effects of electrostatic charging and finite energy resolution were also experimentally precluded from affecting the data in any appreciable way. While peaks A (at $(\pi/2, \pi/2)$) and B (at $(\pi, 0)$), primarily of $J_{\text{eff}} = 1/2$ character, clearly shift to higher binding energy with decreasing temperature below T_N , peak C (at (π, π)), primarily of $J_{\text{eff}} = 3/2$ character, does not show any appreciable change in position. These observed spectral features can be suitably fit with a single Gaussian throughout the entire temperature range. In Fig. 7(b) we show the temperature dependence of the peak position and width quantitatively determined by our fits at the positions A–C. The peak positions at A and B on the $J_{\text{eff}} = 1/2$ band show an energy shift of about 40 meV in total below T_N , then abruptly stop shifting above T_N , while C on the $J_{\text{eff}} = 3/2$ shows negligible changes. Furthermore, the linewidth broadens continuously at a rate of ~ 0.2 meV/K with increasing temperature, again expected from the thermal excitations of the bosonic dressing observed in polaronic systems such as Sr_2IrO_4 and the undoped cuprates.^{22,23} This unusual temperature dependence of the peak position suggests that only the $J_{\text{eff}} = 1/2$ band, which drives the insulator-metal transition, responds dramatically to the presence of long-range antiferromagnetism, while the $J_{\text{eff}} = 3/2$ states, which are nearby in energy, do not respond appreciably to the onset of the long-range antiferromagnetic order. The single particle excitation gap is directly enhanced by the presence of antiferromagnetic order, which would not be expected in simple Mott insulators, but suggestive of a Slater insulator, where the charge gap is directly tied to spin-density wave order. Structural origins of such a shift can be ruled out, as no sudden changes in the LEED patterns or in the crystal symmetry or lattice parameters have been observed either in Ba_2IrO_4 or Sr_2IrO_4 with temperature.^{13,25,26}

The clear persistence of the gap and insulating behavior above T_N obviously indicates

that the system does not behave as a simple Slater insulator. Furthermore, the nonmonotonic change of the observed $J_{\text{eff}} = 1/2$ states through T_N suggests the possibility that the effective Coulomb interactions may be enhanced below T_N accompanied by an ordering of the local moments. For example, in the antiferromagnetic Mott insulator LaTiO_3 , a similar nonmonotonic change of the Mott gap through T_N has been reported.³⁰

In Fig. 8(a) we illustrate schematically the temperature evolution of the gapped $J_{\text{eff}} = 1/2$ dispersion observed in Ba_2IrO_4 . While the charge gap continues to soften when approaching T_N , it does not collapse above T_N , reflecting the robust correlated insulating state. On the other hand, the magnitude of the gap itself is relatively small and the bandwidth is found to be barely renormalized relative to the predictions from density functional theory, as schematically shown in Fig. 8(c). This is in stark contrast to conventional $3d$ transition metal oxide Mott insulators which feature a much larger charge gap and a more strongly renormalized bandwidth (Fig. 8(d)), a clear distinction between the parent insulating state of the layered iridates versus the cuprates. When the spin-orbit interaction is sufficiently strong, even a modest Coulomb repulsion is sufficient to push the nearly fully occupied $J_{\text{eff}} = 3/2$ band below E_F (blue), while splitting the half-filled $J_{\text{eff}} = 1/2$ band (orange).

V. CONCLUSION

In summary, we have investigated the electronic ground state and its temperature evolution in Ba_2IrO_4 using a combination of reactive oxide molecular beam epitaxy and angle-resolved photoemission spectroscopy. A comparison between the experimental data and theoretical calculations have demonstrated the importance of the $J_{\text{eff}} = 3/2$ states for accurately describing the low-energy electronic structure. Our measurements have revealed that while the $J_{\text{eff}} = 1/2$ and $3/2$ bands are barely renormalized relative to the band structure calculations, the two bands exhibit an unusual dichotomy in their behavior through the Néel transition. Only the split $J_{\text{eff}} = 1/2$ subband shows a substantial softening of the gap with increasing temperature approaching T_N , suggesting an important role of the antiferromagnetic ordering in the formation of the insulating phase, while the gap itself remains robust well into the paramagnetic state. This surprising contrast in the behavior of the low-energy $J_{\text{eff}} = 1/2$ and $3/2$ states should be crucial in developing accurate effective low-energy models to describe the parent insulating layered iridates and any emergent ground states, such

as exotic superconductivity, that may be realized upon carrier doping.

Acknowledgments

We gratefully acknowledge insightful discussions with J. W. Freeland, J. H. Lee, and T. Senthil. In particular, we would like to thank M. Gioni for helpful discussions regarding previously unpublished data in Ref. 24, which we became aware of during the preparation of this manuscript. This work was supported by the Air Force Office of Scientific Research (Grant No. FA9550-11-1-0033 and FA9550-12-1-0035), and the National Science Foundation through the MRSEC program (Cornell Center for Materials Research, DMR-1120296). M.U. acknowledges the support by JSPS Postdoctoral Fellowships for Research Abroad.

* Present address: Department of Applied Physics and Quantum-Phase Electronics Center (QPEC), University of Tokyo, Tokyo 113-8656, Japan

† Author to whom correspondence should be addressed: kmshen@cornell.edu

- ¹ X. Wan, A.M. Turner, A. Vishwanath, and S.Y. Savrasov, *Phys. Rev. B* **83**, 205101 (2011).
- ² W. Witczak-Krempa and Y.B. Kim, *Phys. Rev. B* **85**, 045124 (2012).
- ³ D. Pesin and L. Balents, *Nat. Phys.* **6**, 376 (2010).
- ⁴ X. Zhang, H. Zhang, J. Wang, C. Felser, and S.-C. Zhang, *Science* **335**, 1464-1466 (2012).
- ⁵ F. Wang and T. Senthil, *Phys. Rev. Lett.* **106**, 136402 (2011).
- ⁶ H. Watanabe, T. Shirakawa, and S. Yunoki, *Phys. Rev. Lett.* **110**, 027002 (2013).
- ⁷ B. J. Kim, H. Jin, S. J. Moon, J. -Y. Kim, B. -G. Park, C. S. Leem, J. Yu, T. W. Noh, C. Kim, S. -J. Oh, J. -H. Park, V. Durairaj, G. Cao, and E. Rotenberg, *Phys. Rev. Lett.* **101**, 076402 (2008).
- ⁸ B. J. Kim, H. Ohsumi, T. Komesu, S. Sakai, T. Morita, H. Takagi, and T. Arima, *Science* **323**, 1329 (2009).
- ⁹ S. J. Moon, H. Jin, W. S. Choi, J. S. Lee, S. S. A. Seo, J. Yu, G. Cao, T. W. Noh, and Y. S. Lee, *Phys. Rev. B* **80**, 195110 (2009).
- ¹⁰ D. Hsieh, F. Mahmood, D. H. Torchinsky, G. Cao, and N. Gedik, *Phys. Rev. B* **86**, 035128 (2012).

- ¹¹ R. Arita, J. Kuneš, A. V. Kozhevnikov, A. G. Eguiluz, and M. Imada, *Phys. Rev. Lett.* **108**, 086403 (2012).
- ¹² Q. Li, G. Cao, S. Okamoto, J. Yi, W. Lin, B. C. Sales, J. Yan, R. Arita, J. Kunes, A. V. Kozhevnikov, A. G. Eguiluz, M. Imada, Z. Gai, M. Pan, and D. G. Mandrus, *Sci. Rep.* **3**, 3073 (2013).
- ¹³ H. Okabe, M. Isobe, E. Takayama-Muromachi, A. Koda, S. Takeshita, M. Hiraishi, M. Miyazaki, R. Kadono, Y. Miyake, and J. Akimitsu, *Phys. Rev. B* **83**, 155118 (2011).
- ¹⁴ S. Boseggia, R. Springell, H. C. Walker, H. M. Rønnow, Ch. Rüegg, H. Okabe, M. Isobe, R. S. Perry, S. P. Collins, and D. F. McMorrow, *Phys. Rev. Lett.* **110**, 117207 (2013).
- ¹⁵ H. Okabe, M. Isobe, E. Takayama-Muromachi, N. Takeshita, and J. Akimitsu, *Phys. Rev. B* **88**, 075137 (2013).
- ¹⁶ H. Okabe, N. Takeshita, M. Isobe, E. Takayama-Muromachi, T. Muranaka, and J. Akimitsu, *Phys. Rev. B* **84**, 115127 (2011).
- ¹⁷ E. H. P. Cordfunke and G. Meyer, *Recueil des Travaux Chimiques des Pays-Bas* **81**, 495-504 (1962).
- ¹⁸ P. Blaha, K. Schwarz, G. Madsen, D. Kvasnicka, and J. Luitz, Wien2k package, available at [http:// www.wien2k.at](http://www.wien2k.at).
- ¹⁹ J. P. Perdew, K. Burke, and M. Ernzerhof, *Phys. Rev. Lett.* **77**, 3865 (1996).
- ²⁰ C. Martins, M. Aichhorn, L. Vaugier, and S. Biermann, *Phys. Rev. Lett.* **107**, 266404 (2011).
- ²¹ H. Watanabe, T. Shirakawa, and S. Yunoki, *Phys. Rev. Lett.* **105**, 216410 (2010).
- ²² K. M. Shen, F. Ronning, W. Meevasana, D. H. Lu, N. J. C. Ingle, F. Baumberger, W. S. Lee, L. L. Miller, Y. Kohsaka, M. Azuma, M. Takano, H. Takagi, and Z.-X. Shen, *Phys. Rev. B* **75**, 075115 (2007).
- ²³ P. D. C. King, T. Takayama, A. Tamai, E. Rozbicki, S. M. Walker, M. Shi, L. Patthey, R. G. Moore, D. Lu, K. M. Shen, H. Takagi, and F. Baumberger, *Phys. Rev. B* **87**, 241106(R) (2013).
- ²⁴ S. Moser, L. Moreschini, A. Ebrahimi, B. D. Piazza, M. Isobe, H. Okabe, J. Akimitsu, V. V. Mazurenko, K. S. Kim, A. Bostwick, E. Rotenberg, J. Chang, H. M. Rønnow, and M. Grioni, *New J. Phys.* **16**, 013008 (2014).
- ²⁵ M. K. Crawford, M. A. Subramanian, R. L. Harlow, J. A. Fernandez-Baca, Z. R. Wang, and D. C. Johnston *Phys. Rev. B* **49**, 9198 (1994).
- ²⁶ Q. Huang, J. L. Soubeyroux, O. Chmaissem, I. Natali Sora, A. Santoro, R. J. Cava, J. J.

Krajewski, and W. F. Peck Jr., J. Solid State Chem. **112**, 355 (1994).

- ²⁷ See Supplemental Material at [URL will be inserted by publisher] for more information regarding tight binding calculation.
- ²⁸ R. Comin, G. Levy, B. Ludbrook, Z.-H. Zhu, C. N. Veenstra, J. A. Rosen, Y. Singh, P. Gegenwart, D. Stricker, J. N. Hancock, D. van der Marel, I. S. Elfimov, and A. Damascelli, Phys. Rev. Lett. **109**, 266406 (2012).
- ²⁹ Q. Wang, Y. Cao, J. A. Waugh, S. R. Park, T. F. Qi, O. B. Korneta, G. Cao, and D. S. Dessau, Phys. Rev. B **87**, 245109 (2013).
- ³⁰ P. Lunkenheimer, T. Rudolf, J. Hemberger, A. Pimenov, S. Tachos, F. Lichtenberg, and A. Loidl, Phys. Rev. B **68**, 245108 (2003).

Figures

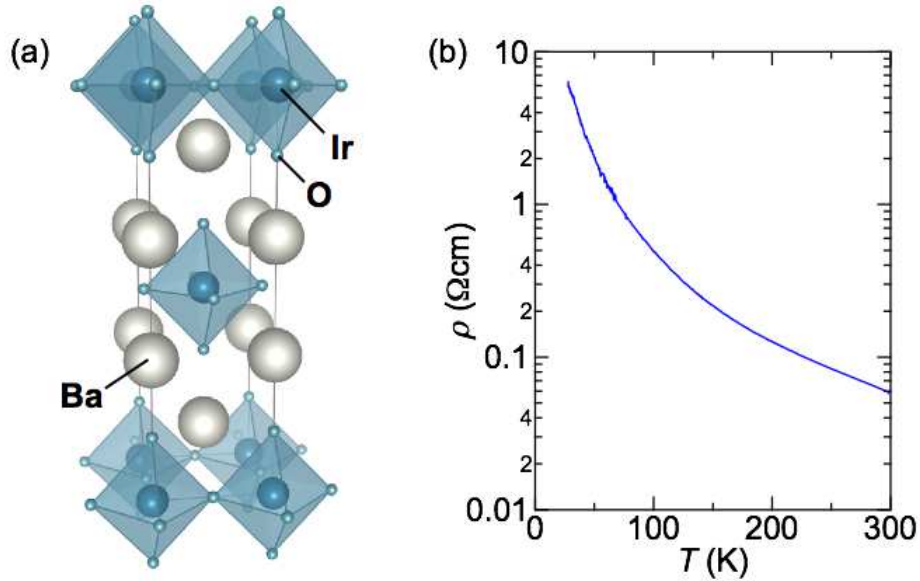


FIG. 1: (Color online) (a) Structure view of Ba₂IrO₄. (b) Temperature dependence of the longitudinal in-plane resistivity of a 16 nm Ba₂IrO₄ film grown on PrScO₃.

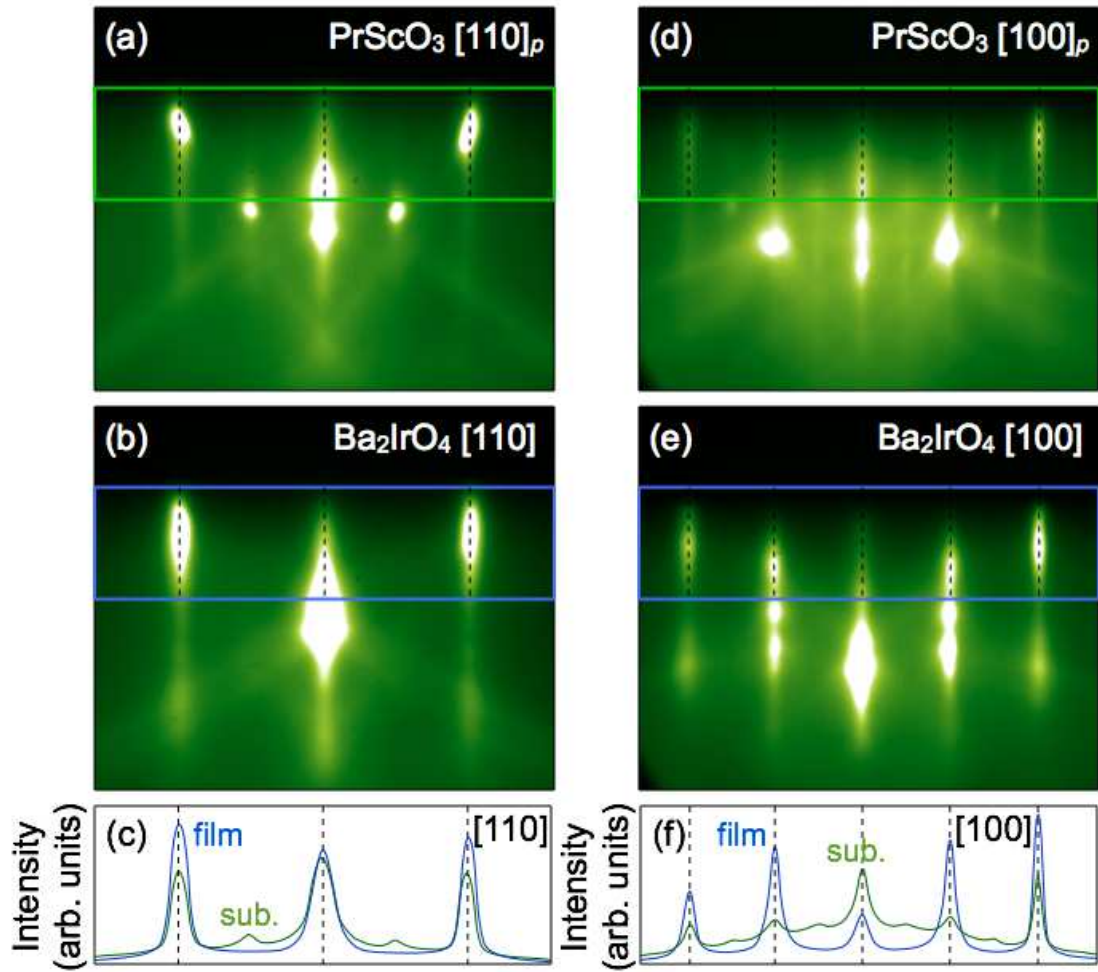


FIG. 2: (Color online) RHEED images of (a) the bare PrScO₃ substrate and (b) after the growth of a 16 nm thick Ba₂IrO₄ film, taken along the [110]_(p) azimuthal direction. (c) RHEED intensity curves integrated within each rectangle window. (d)-(f) The results for the [100]_(p) direction.

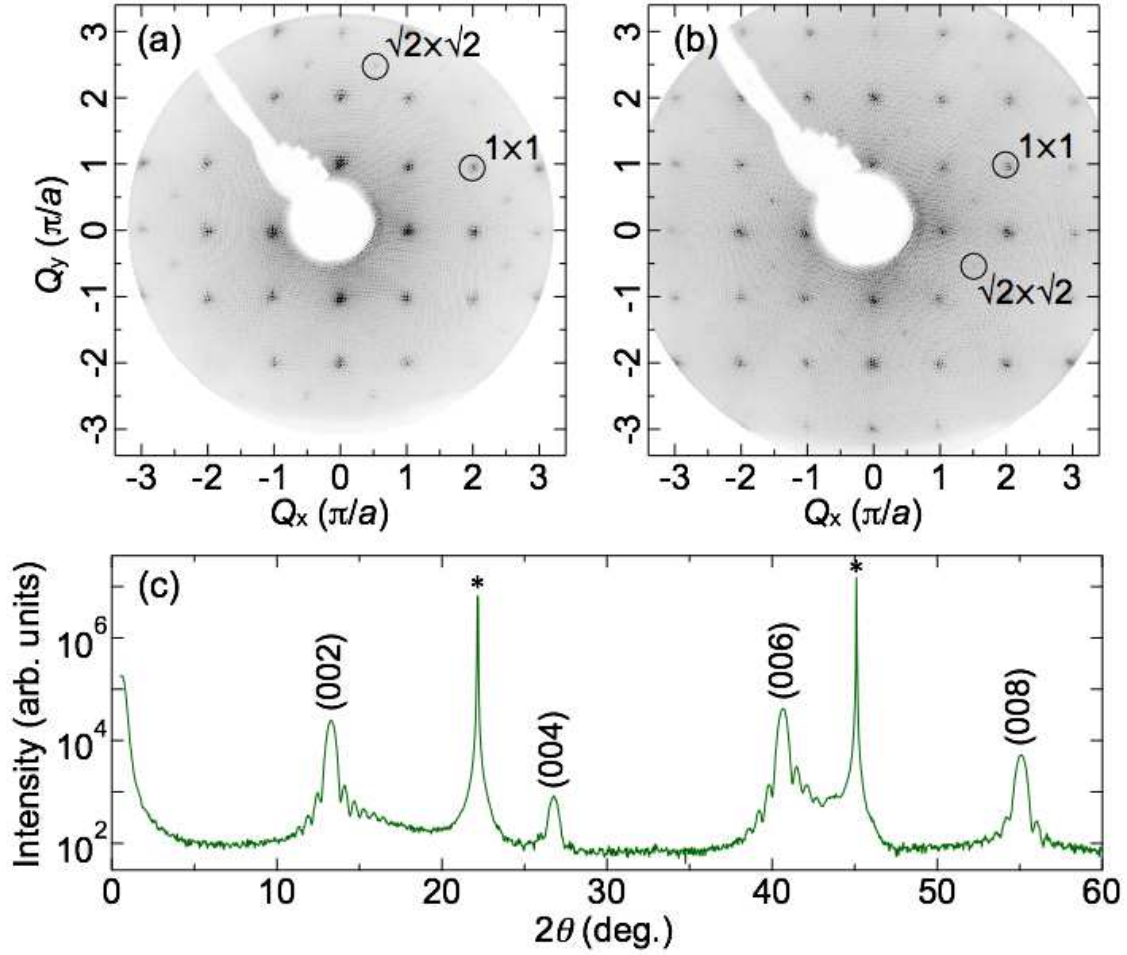


FIG. 3: (Color online) LEED images of a Ba_2IrO_4 film, taken along the $[001]$ direction with an electron energy of (a) 150 and (b) 200 eV. (c) XRD $\theta-2\theta$ scan of a 16 nm thick Ba_2IrO_4 film grown on PrScO_3 substrate. Substrate peaks are marked with an asterisk.

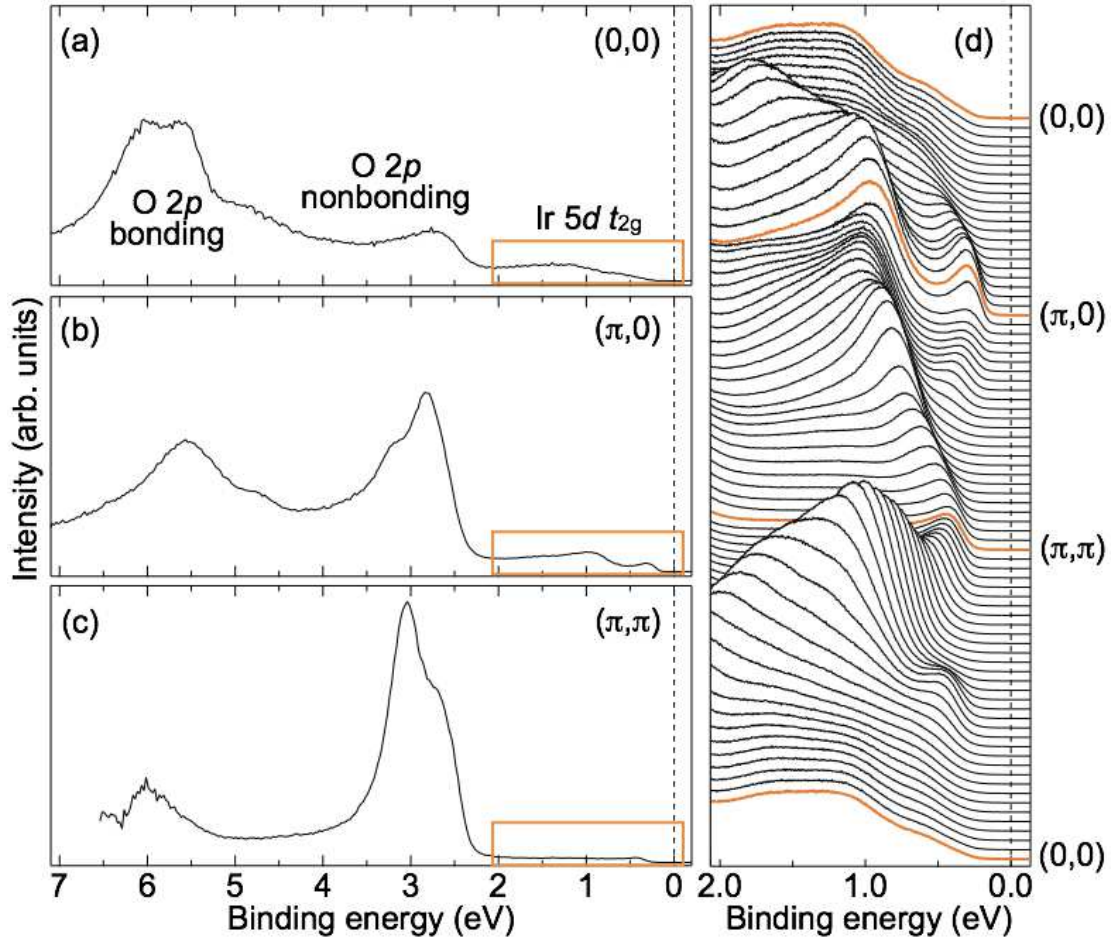


FIG. 4: (Color online) Valence band photoemission spectra at (a) $(0,0)$, (b) $(\pi,0)$, and (c) (π,π) points for Ba_2IrO_4 , respectively, taken at 100 K to prevent charging, showing Ir $5d t_{2g}$ bands and O $2p$ bonding and nonbonding states at higher binding energies. (d) Magnified low-energy electronic structures along $(0,0) \rightarrow (\pi,0) \rightarrow (\pi,\pi) \rightarrow (0,0)$ high-symmetry lines of the tetragonal Brillouin zone.

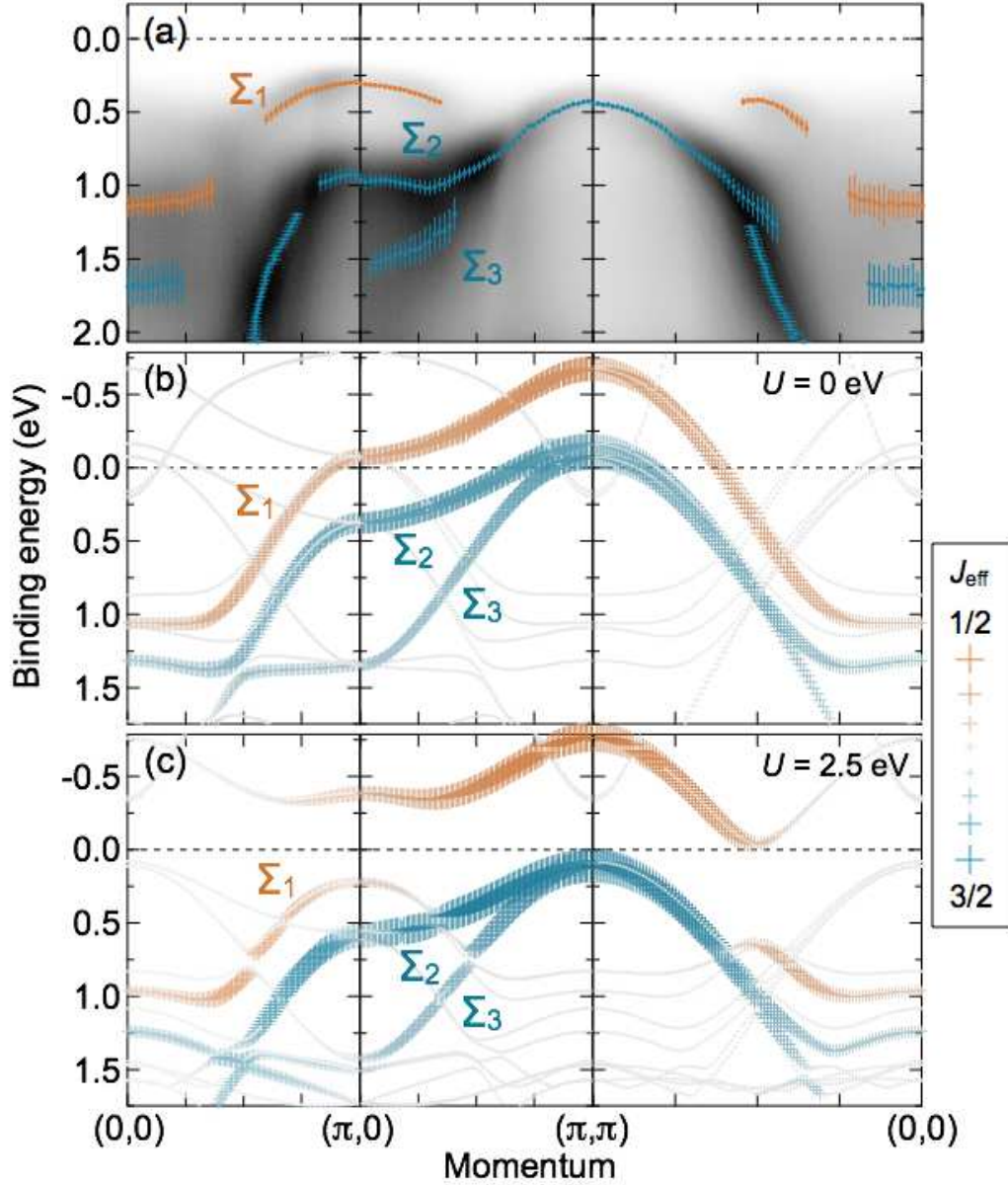


FIG. 5: (Color online) (a) Near- E_F ARPES spectral intensity plot along high-symmetry directions, taken at 100 K. Extracted EDC and MDC peak positions are overlaid with circles with error bars. DFT calculations including the spin-orbit coupling with U of (b) 0 and (c) 2.5 eV. The J_{eff} character is calculated by projecting the eigenstates onto the $J_{\text{eff}} = 1/2$ and $3/2$ bases in the atomic limit.

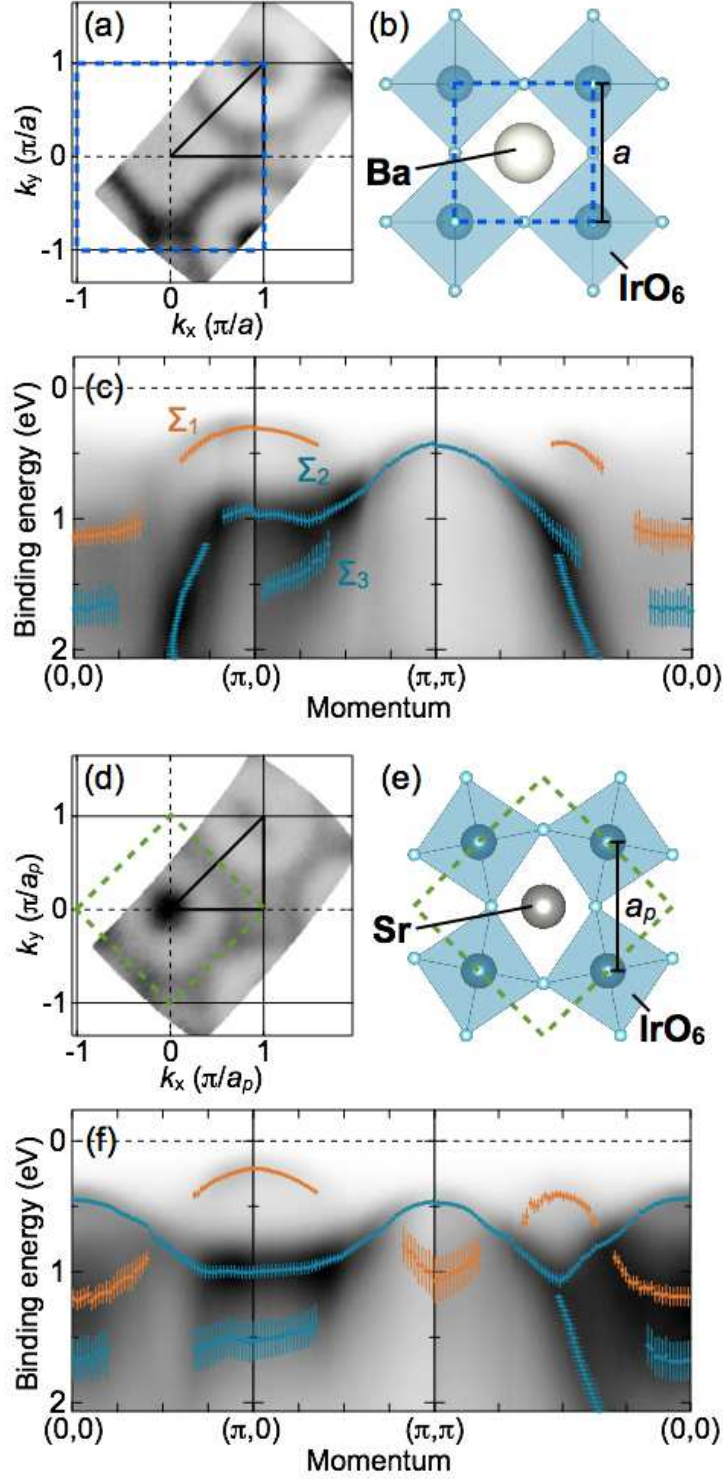


FIG. 6: (Color online) (a) Unsymmetrized isoenergy map at 0.4 ± 0.005 eV binding energy, (b) crystal structure projected on (001), and (c) E versus k spectra along high-symmetry lines for Ba₂IrO₄. Dashed squares in (a) and (b) indicate the in-plane Brillouin zone and unit cell, respectively. (d)-(f) The corresponding data from a Sr₂IrO₄ thin film grown on LSAT is shown for comparison.

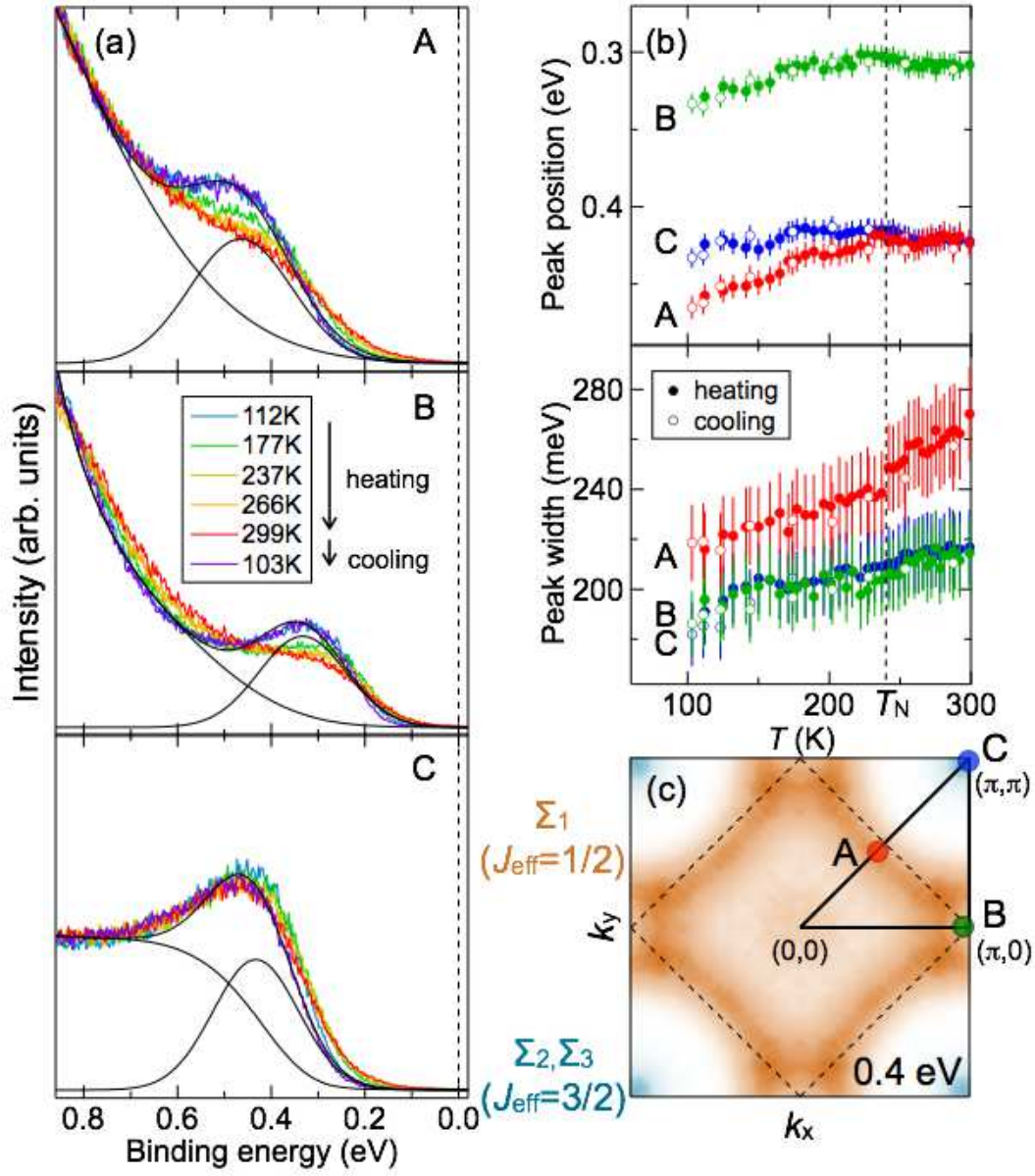


FIG. 7: (Color online) (a) Temperature-dependent EDCs at momentum positions $A \sim (\pi/2, \pi/2)$, $B \sim (\pi, 0)$, and $C \sim (\pi, \pi)$ as sketched in (c). The spectra were measured by cycling samples from 112 K to 299 K and then back to 103 K. Fitting results (one Gaussian curve and a background) for 103 K data are also represented by black curves. (b) Temperature evolution of the peak position (upper panel) and width (lower panel) for A–C. (c) Symmetrized isoenergy map at 0.4 eV in the full Brillouin zone, integrated within a ± 5 meV window.

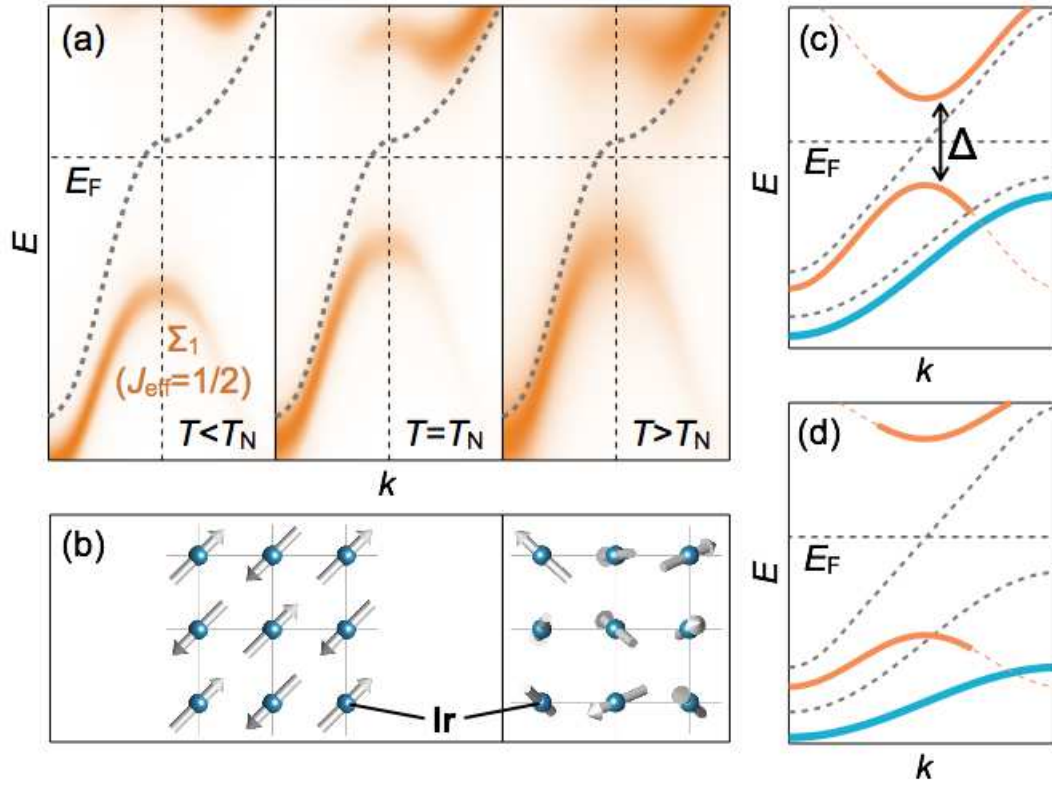


FIG. 8: (Color online) Schematic illustration of the temperature dependence of (a) the near- E_F band dispersion and (b) the in-plane spin state in Ba_2IrO_4 . Dashed curves represent the original branch without including the electron correlation. Energy dispersions affected by (c) weak or (d) strong correlation are also shown.